ACS APPLIED MATERIALS & INTERFACES

Research Article

www.acsami.org

$La_{0.8}Sr_{0.2}MnO_3$-Based Perovskite Nanoparticles with the A-Site Deficiency as High Performance Bifunctional Oxygen Catalyst in Alkaline Solution

Litao Yan,[†] Yue Lin,[‡] Xue Yu,[†,§] Weichuan Xu,[†] Thomas Salas,[†] Hugh Smallidge,[†] Meng Zhou,[*,†] and Hongmei Luo[*,†]

[†]Department of Chemical and Materials Engineering, New Mexico State University, Las Cruces, New Mexico 88003, United States

[‡]Hefei National Laboratory for Physical Sciences at the Microscale, University of Science and Technology of China, Hefei, Anhui 230026, China

[§]Department of Materials Science and Engineering, Kunming University of Science and Technology, Kunming, Yunnan 650093, China

Supporting Information

ABSTRACT: Perovskite $(La_{0.8}Sr_{0.2})_{1-x}Mn_{1-x}Ir_xO_3$ (x = 0 (LSM) and 0.05 (LSMI)) nanoparticles with particle size of 20−50 nm are prepared by the polymer-assisted chemical solution method and demonstrated as high performance bifunctional oxygen catalyst in alkaline solution. As compared with LSM, LSMI with the A-site deficiency and the B-site iridium (Ir)-doping has a larger lattice, lower valence state of transition metal, and weaker metal−OH bonding; therefore, it increases the concentration of oxygen vacancy and enhances both oxygen evolution reaction (OER) and oxygen reduction reaction (ORR). LSMI exhibits superior ORR performance with only 30 mV onset potential difference from the commercial Pt/C catalyst and significant enhancement in electrocatalytic activity in the OER process, resulting in the best oxygen electrode material among all the reported perovskite oxides. LSMI also exhibits high durability for both ORR (only 18 mV negative shift for the half-wave potential compared with the initial ORR) and OER process with 10% decay. The electrochemical results indicate that the A-site deficiency and Ir-doping in perovskite oxides could be promising catalysts for the applications in fuel cells, metal−air batteries, and solar fuel synthesis.

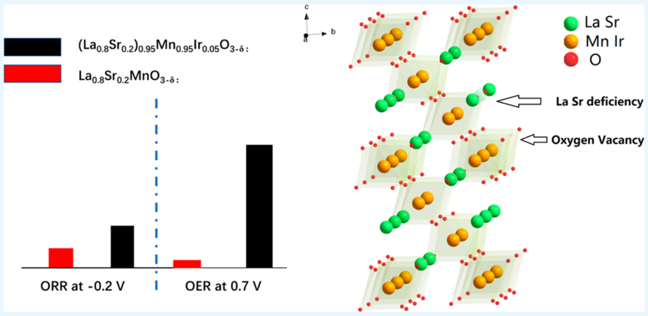

KEYWORDS: *$La_{0.8}Sr_{0.2}MnO_3$, perovskite, oxygen reduction reaction, oxygen evolution reaction, A-site deficiency, Ir-doping*

1. INTRODUCTION

Recently, clean, green, efficient, and sustainable electrochemical devices for energy storage and conversion have been extensively investigated because of the huge consumption of nonrenewable fossil fuels. The emission of greenhouse gas from the burning of fossil fuel brings about environmental issues.[1−4] Oxygen evolution reaction (OER), which can produce oxygen by effective oxidation of water, is considered as an effective catalysis to convert electricity to chemical energy.[3,5−13] Metal−air batteries, a typical new generation electrochemical device, have stimulated to efficient electrocatalyst development.[3,11,14−18] However, it is a big challenge to make the electrochemical water oxidation process more economically attractive because of high overpotential and thereby energy losses at the air-breathing electrode.[8,19,20] The OER process in alkaline solution with the four-electron transfer takes place by the following equation:[12,21]

$$4OH^- \rightarrow O_2 + 2H_2O + 4e^- \quad (1)$$

The oxygen reduction reaction (ORR), a reversible reaction of OER, also evolved in high overpotential in fuel cell and metal−air batteries.[3,10,16,22] Recently, developing an electrochemical catalyst with high ORR and OER activities in alkaline solution became a hot topic in fuel cell and electrolysis technology.[23,24] For example, Zhao et al. reported that ammonia-treated Co_3O_4 and carbon nanotubes exhibited high OER and ORR.[23] Graphene nanotubes have been demonstrated as superior bifunctional catalysts in alkaline solution.[24] Both ORR and OER performances for graphene nanotubes are comparable to the state-of-art catalysts, for example, Pt/C for ORR and IrO_2 for OER.[24] ABO_3 perovskite oxides have been extensively investigated as bifunctional catalysts because of their high versatility in compositions and electronic structure.[25,26] Jin et al. developed $Ba_{0.9}Co_{0.5}Fe_{0.4}Nb_{0.1}O_{3-\delta}$ perovskite oxide as a

Received: May 9, 2017
Accepted: June 29, 2017
Published: June 29, 2017

DOI: 10.1021/acsami.7b06458
ACS Appl. Mater. Interfaces 2017, 9, 23820−23827

bifunctional catalyst for ORR and OER; however, both activities are far less than that of the state-of-art catalysts.[27] Oxygen vacancy in perovskite oxide plays an important role in the electrochemical properties toward OER and ORR. The creation of oxygen vacancy is always accompanied by the change of the valence state and electronic structure of transition metal.[28,29] The covalency between the transition metal 3d-band and the oxygen 2p-band depends on the degree of oxygen vacancy. The higher oxygen vacancy concentration leads to higher transition metal−oxygen covalency for enhanced electrocatalytic activies.[28]

Creating the A-site deficiency in ABO_3 perovskite is an effective approach to induce oxygen vacancy and modify the electronic structure, resulting in the improved electrochemical catalytic properties. The equation of creating A-deficiency is described by the following:

$$\mathrm{LaBO_3} \xrightarrow{\text{A-deficiency}} \mathrm{V_{La}'''} + 3\mathrm{B_B} + 3\mathrm{O_O^X} \xrightarrow{-\mathrm{O_2}} \mathrm{V_{La}''{}'} + 3\mathrm{B_B^{\mathit{x}}} + \frac{3}{2}\mathrm{V_{\ddot{O}}}$$

$LaFeO_{3-\delta}$ with the A-site deficiency owned the best functionality for both OER and ORR due to the creation of oxygen vacancy and a small amount of Fe^{4+} species.[30] However, the electrochemical performance is still lower than that of the state-of-art catalyst, e.g., 0.8 V onset potential for the A-deficiency $LaFeO_{3-\delta}$ while 0.95 V for Pt/C.[30] In addition to creating A-deficiency, doping (e.g., cobalt, nickel, and iron) to the B-site of ABO_3 crystal structure is considered as a convincing strategy to easily modify the electronic structure and then subsequently enhance the electrochemical properties.[31,32] Furthermore, engineering the particle size of perovskite oxides is expected to improve the OER and ORR activities. As compared with their bulk counterparts, it has been demonstrated that the enhanced electrochemical performance of $LaCoO_3$ nanoparticles including lower overpotential and smaller Tafel slope was mainly attributed to the increased reactivity of the active sites because the spin-state transition from the low-spin state to the high-spin state of Co^{3+} ions induced the change of the orbital e_g-filling of Co^{3+} from 1.0 to 1.2.[33] However, it is a challenge to reduce the perovskite oxide particle size to nanoscale for meeting the requirement of optimized e_g-filling.

Recently, we have developed a polymer-assisted chemical solution method (PACS) to prepare a phosphor europium-doped yttrium vanadate (YVO_4:Eu) nanoparticle network after high annealing temperature.[34] In PACS, water-soluble polymers ethylenediaminetetraacetic acid (EDTA) and polyethylenimine (PEI) are used to stabilize metal ions and to control the stability of the solution.[34] The PACS method is a relatively simple and inexpensive process that enables the formation of a range of metal-oxide nanomaterials. In this paper, $(La_{0.8}Sr_{0.2})_{1-x}Mn_{1-x}Ir_xO_3$ (LSM for $x = 0$ and LSMI for $x = 0.05$) nanoparticles with particle size of less than 50 nm are successfully synthesized by PACS and developed as superior bifunctional catalysts in alkaline solution. LSM and its associated oxides have been reported as the highest ORR catalyst among the perovskite oxides.[18,25] However, OER for LSM should be improved for bifunctional catalyst as compared with other high performance OER catalysts.[26] The LSMI catalyst we designed in this paper takes the advantages of smaller particle size, the A-site deficiency, and B-site doping. The incorporation of the A-deficiency and Ir-doping is predicted to achieve higher oxygen vacancy concentration and boost both OER and ORR. The onset potential of LSMI for ORR is around −0.05 V vs Ag/AgCl, only 30 mV negative shifting from the commercial Pt/C catalyst, while the onset potential for OER is around 0.48 V vs Ag/AgCl, which is comparable to the state-of-art IrO_2 catalyst.

2. MATERIALS AND METHODS

2.1. Materials Synthesis. Polymers consisting of ethylenediaminetetraacetic acid (EDTA) and polyethylenimine (PEI) were dissolved in 10 mL of DI water. Appropriate amounts of lanthanum nitrate, strontium nitrate, manganese acetate, and iridium chloride for two samples $(La_{0.8}Sr_{0.2})_{1-x}Mn_{1-x}Ir_xO_3$ ($x = 0$ (LSM) and 0.05 (LSMI)) were mixed with polymer solutions. The weight ratio of EDTA, PEI, and metal precursors is around 1:1:1. After stirring for 1 h, uniform metal−polymer solution was formed. The solution was heated at 650 °C in air to get LSM and LSMI nanoparticles.

2.2. Material Characterization. The resulting LSM and LSMI perovskite oxides were characterized by X-ray diffraction (XRD, Rigaku Miniex-II with Cu Kα (1.5406 Å) radiation, 30 kV and 15 mA) to identify the phase and crystal structure. The structure was further demonstrated by the selected area electron diffraction (SAED) patterns. The morphology of LSM and LSMI was characterized by a field emission scanning electron microscope (FESEM) (JEOL, model JSM-7600F) and a transmission electron microscope (TEM) (JEOL, model JEM- 2100) operating at 200 kV. The valence states of the manganese, iridium, and oxygen were evaluated by X-ray photoelectron spectroscopy (XPS, Thermo K-Alpha spectrometer equipped with a monochromatic Al Kα X-ray source). High-angle annular dark-field scanning transmission electron microscopy (HAADF-STEM) and energy dispersive spectroscopy (EDS) mapping images were used to characterize the elemental distribution (JEOL JEM-ARF200F). The Brunauer−Emmett−Teller (BET) surface area of LSMI was recorded by a Micromeritics ASAP 2050 using the standard N_2 adsorption and desorption isotherm measurement at 77 K.

2.3. Electrochemical Characterization. Electrochemical experiments were carried out in a typical three-electrode electrochemical cell with a water jacket. The catalyst was loaded on the rotating disk electrode (RDE) with a 5.0 mm diameter glassy carbon, and the loading weight of LSM and LSMI was around 0.2 mg cm^{-2}. Pt wire and Ag/AgCl electrode (Pine Research Instruments) were used as the counter and the reference electrodes, respectively. The electrolyte used in the electrochemical test was oxygen-saturated 0.1 M potassium hydroxide (KOH) solution (Sigma-Aldrich). Cyclic voltammetry was performed in the above electrolyte at a scan rate of 50 mV s^{-1}. Polarization curves for the oxygen reduction reaction (at different rotation speeds of 100, 400, 900, and 1600 rpm) and oxygen evolution reaction (at a rotation speed of 1600 rpm) were tested in the electrolyte using a CHI electrochemical instrument at scan rates of 5 and 20 mV s^{-1}, respectively. The *iR* correction was performed to compensate for the effect of solution for all potential values. The potential values were calculated by the following equation after the *iR* correction: $E_{iR\,\mathrm{corrected}} = E - iR$, where i is the measured current density and R the ohmic resistance of electrolyte (∼49 Ω), which was measured by ac impedance in 0.1 M KOH. The resistance for the LSMI catalyst was characterized by electrochemical impedance spectra (EIS) at 0.6 V vs Ag/AgCl with frequencies range from 100 kHz to 0.1 Hz under an ac voltage of 5 mV. The resistance test for LSM was performed at four different potentials of 0.6, 0.7, 0.8, and 0.9 V vs Ag/AgCl. The kinetic parameters including the electron transfer number and the kinetic current density in ORR can be determined from the following Koutecky−Levich (K−L) equation:[31]

$$\frac{1}{J} = \frac{1}{J_k} + \frac{1}{J_L} = \frac{1}{nFkC^O} + \frac{1}{0.62nFD_{O_2}{}^{2/3}\nu^{-1/6}C^O w^{1/2}}$$

where J, J_k, and J_L are associated with the measured current density as well as the kinetic and diffusion-limiting current densities, respectively. In this equation, n is the electron transfer number and F is the Faraday constant. C^O, D_{O_2}, w, ν, and k are the concentration of oxygen, the diffusion coefficient of oxygen, the rotating rate of the rotating

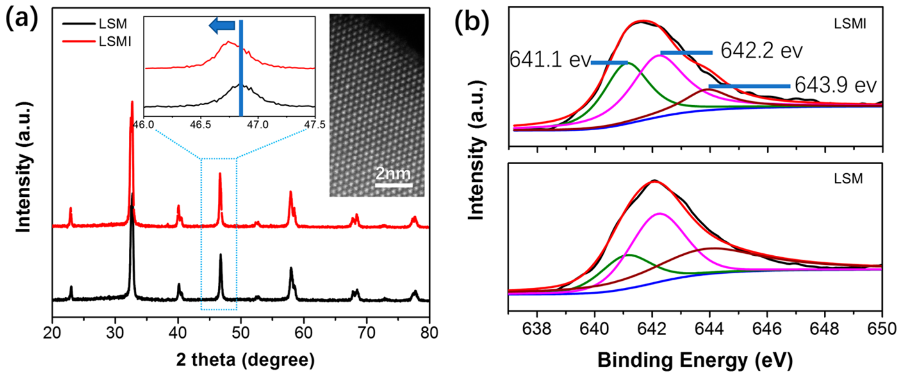

Figure 1. (a) XRD patterns of LSM and LSMI (inset pictures: left, the enlarged XRD patterns of LSM and LSMI from 46 and 47.5°; right, HADDF-STEM image of LSMI). (b) Mn XPS patterns of LSM and LSMI.

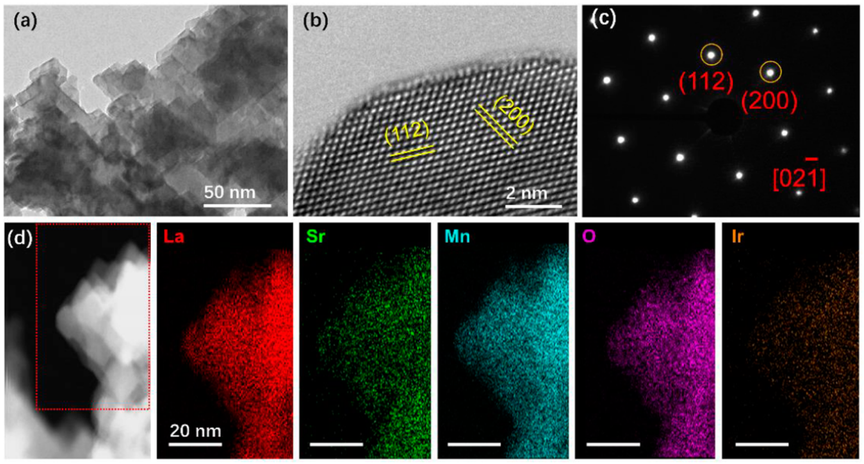

Figure 2. (a) TEM image, (b) HRTEM, (c) SAED of LSMI, and (d) HAADF EDX mapping of LSMI with the elemental mapping of La, Sr, Mn, O, and Ir.

electrode (rad s^{-1}), the kinetic viscosity of the oxygen-saturated 0.1 M KOH, and the rate constant for oxygen reduction reaction, respectively.

3. RESULTS AND DISCUSSION

The phase and crystal structure of LSM and LSMI were analyzed by XRD, as shown in Figure 1a. As you can see, both LSM and LSMI with A-deficiency and Ir-doping can become single phase, which is also proved by the clearly distributed atoms in the HAADF-STEM image (inset picture in Figure 1a). Figure S1 presents the XRD Rietveld refinement of LSMI. The reliability of the Rietveld refinement is satisfactory regarding the goodness of fit. Both LSM and LSMI have the same orthorhombic structure. The lattice parameters are a = 5.453 Å, b = 5.504 Å, c = 7.761 Å for LSM and a = 5.460 Å, b = 5.501 Å, c = 7.769 Å for LSMI. The slightly expanded lattice parameters are consistent with the negative shift of XRD peaks for LSMI as compared with LSM (inset in Figure 1a). The A-deficiency $LaFeO_{3-\delta}$ had the contracted lattice parameters while the A-deficiency $La_{0.6}Sr_{0.4}Co_{0.2}Fe_{0.8}O_{3-\delta}$ led to the expanded lattice.[30,35] The contradictory results indicated that the concentration of oxygen vacancy is an important effect on the lattice parameters. The loss of oxygen in crystal structure could lead to the decrease in the valence state of transition metal, resulting in the lattice expansion.[36,37] In other words, the expanded lattice may indicate higher oxygen vacancy in LSMI compared with LSM. Besides, the radius of Ir^{4+} (76 pm) is higher than that of Mn^{3+} (72 pm, 6-coordinate, octahedral); Ir-doping is also assumed for the lattice expansion.

The electrochemical behavior of perovskite oxides is strongly dependent on the valence state of transition metal and oxygen vacancy on the surface of the catalysts. Therefore, XPS was performed, and the XPS spectra of LSM and LSMI are displayed in Figure S2. The two peaks at around ~642 and ~653 eV are typical peaks of Mn $2p_{3/2}$ and Mn $2p_{1/2}$. Except for the peaks corresponding to Mn, the peaks corresponding to La, Sr, and O were also detected. Peaks at ~62 and 65 eV corresponding to Ir 4f were observed for LSMI, while no Ir peaks appeared in LSM. High-resolution XPS further provides more details about the valence states of transition metals. The high-resolution XPS of Ir 4f in LSMI is presented in Figure S3. The peak at 64.8 eV corresponds to the valence state of Ir +4, suggesting Ir in the high oxidation state. The high oxidation state of Fe +4 was also reported in the A-deficiency $LaFeO_{3-\delta}$.[30] As shown in Figure 1b, the Mn 2p peak of LSMI shifts toward lower binding energy as compared with LSM, indicating that the valence state of Mn is reduced in LSMI. Three distinct peaks at 641.1, 642.2, and 643.9 eV were found in the Mn $2p_{3/2}$ region. The peaks at 641.1 and 642.2 eV are attributed to the valence states of Mn +3 and Mn +4, respectively. The peak at 643.9 eV corresponds to the manganese species in different coordination environment with other ions such as La^{3+} and Sr^{2+}.[38] The percentages of different valence states of Mn species estimated from the relative area of

DOI: 10.1021/acsami.7b06458
ACS Appl. Mater. Interfaces 2017, 9, 23820−23827

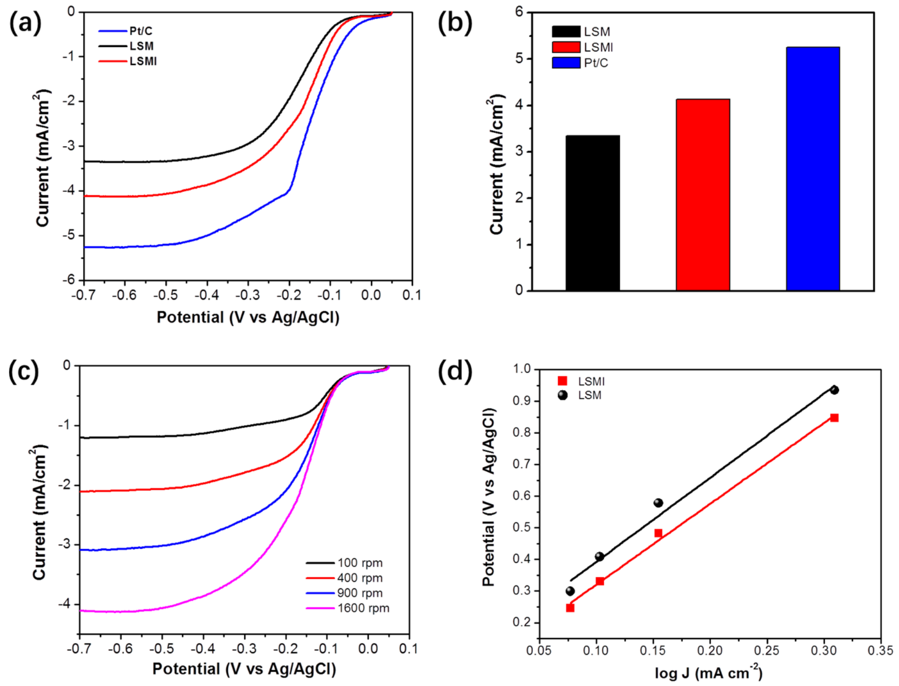

Figure 3. (a) ORR LSVs for Pt/C, LSM, and LSMI. (b) Limited current densities for Pt/C, LSM, and LSMI. (c) ORR LSV profiles for LSMI at different rotation speeds. (d) K−L plots at −0.6 V Ag/AgCl for LSM and LSMI catalysts.

the fitted subpeaks are listed in Table S1. The percentage of Mn species with the low valence state in LSMI (36.87%) is clearly higher than that in LSM (19.05%). The partial reduced Mn valence state in LSMI could be ascribed to balance the high oxidation state of Ir or more oxygen vacancy would be formed.

The strength of bonding between the surface-oxygenated intermediates and the surface active sites of catalyst is suggested to play important roles in the OER activity of perovskite oxides.[7] Metal oxide surface has an affinity for adsorption of OH^- ions when the oxide contacts with alkaline aqueous solution.[12] The electrochemical activity increases with the decreasing M−OH bonding strength.[6,7] The electrons from the d-orbital of the surface transition metal ions may occupy the antibonding orbital of M−OH, indicating that the M−OH bonding strength may decrease as the number of d-electrons increases.[39] It is remarkable that the perovskite oxides can easily lose lattice oxygen atoms to form oxygen vacancy, which can produce the weaker bonding strength between transition metals and oxygenated species. The high oxygen vacancy concentration in the perovskite oxide exhibited enhanced OER performance.[39−44] The density of free carrier increased after the formation of oxygen vacancy, and then the overlap between O_{2p} and M_{3d} occurred, indicating the strong covalency of metal−oxygen bonds to enhance the charge transfer.[42] Finally, the electronic conductivity behavior also significantly influences the charge transfer during the OER process.[31,45−47] Therefore, oxygen vacancy has a remarkable effect on the electronic structure and coordination chemistry, including the number of 3d e_g-orbital electrons and covalence of transition metal−oxygen bond. The high-resolution XPS spectra for O 2p in LSM and LSMI are exhibited in Figure S4; except for the lattice oxygen (~529.2 eV for O^{2-}) observed in both LSM and LSMI, the high oxidation oxygen species on the surface of LSMI is more than that of LSM, which is the dominant species on the surface toward the electrochemical catalytic activity. Therefore, LSMI with A-deficiency and Ir-doping has higher concentration of oxygen vacancy for enhanced electrocatalytic activities.

The morphologies of LSMI and LSM were investigated and are shown in Figure 2a and Figure S5, respectively. TEM images clearly indicate that the LSM and LSMI nanoparticles with particle size of 20−50 nm were obtained. The crystal structure of LSMI was further confirmed by high-resolution HRTEM image (Figure 2b) and the corresponding selected area diffraction pattern (SAED) (Figure 2c). The *d*-spacing of 0.387 nm is associated with LSM (110) plane while the *d*-spacing of 0.274 nm corresponds to the LSMI (200) plane. The slight increase of the lattice of LSMI is in consistent with the XRD result. The compositions of LSMI were characterized with TEM and HAADF-EDX mapping, as displayed in Figure 2d panels. EDX mapping demonstrates that Ir was uniformly distributed in LSMI, and no separated IrO_2 was observed, indicating Ir to occupy the Mn position of LSM. Nevertheless, nanosized PdO particles (8−10 nm) were observed on the surface of Pd-doped $LaFeO_3$.[48] The surface area of LSMI was characterized by N_2 adsorption and desorption (Figure S6). The BET surface area is around 26 $m^2\ g^{-1}$, almost 4 times of that for $LaFeO_{3-\delta}$,[30] benefiting from the smaller particle sizes of LSMI (Figure S7) from our unique PACS method.

The smaller particle size and high surface area would result in more active sites and subsequently increase the electrochemical performance. The PACS method has all the advantages of other chemical solution approaches such as low cost and easy setup. For the PACS process, water-soluble metal salts bind with polymer such as polyethylenimine (PEI). A few metal ions such as Ni and Co bind to PEI directly through covalent bonding between the lone pairs on the nitrogen atoms of the PEI and the metal cations.[49,50] Other metal ions, such as La, Sr, Mn, and Ir, do not bind to PEI directly; ethylenediaminetetraacetic acid (EDTA) is introduced to bind with these metal ions through covalent bonding to form an EDTA−metal complex.[51] Finally, under the drive force of hydrogen bonding and electrostatic

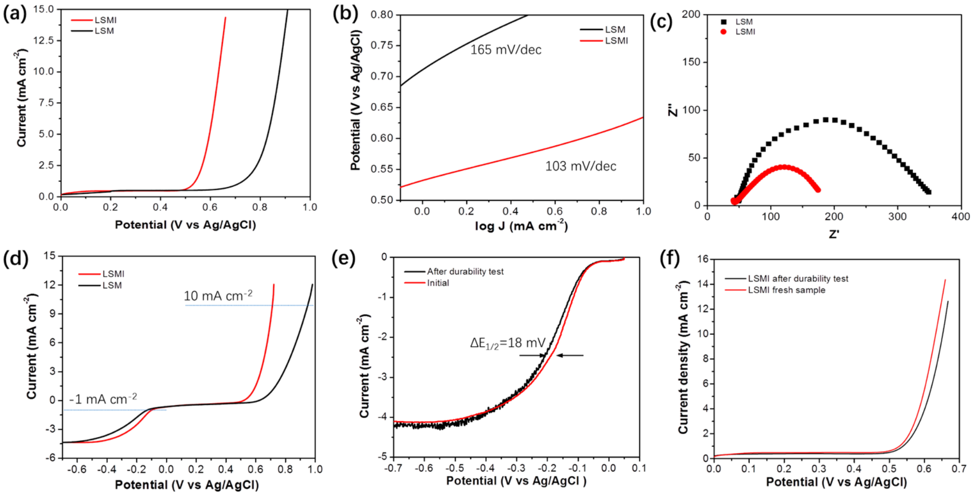

Figure 4. (a) OER LSVs. (b) Tafel plots. (c) EIS spectra. (d) OER and ORR profiles for LSM and LSMI. (e) ORR and (f) OER performances for initial and after durability test for LSMI.

attraction, the EDTA complexes further bind to PEI. The molecular structure of EDTA and PEI and the bonding with transition metal ions are listed in Figure S8. Our recent work demonstrated that the unique solution chemistry of PACS delivered stable and homogeneous solutions at a molecular level that allows formation of high quality thin films and high surface area nanoparticles.[50] The thin carbon coating layer remained on the surface of metal oxides after the incomplete decomposition of the polymer when the solutions were heated at lower temperatures.[52] The existence of carbon layer on metal oxide nanoparticles after heating the sample at 550 °C (Figure S9) can prevent the agglomeration of nanoparticles, leading to metal oxides with smaller particles and high surface area. A small amount of carbon may still exist after annealing the sample at 650 °C, although the HRTEM image (Figure 1a) of LSMI showed no carbon layer. The existence of carbon can further increase the electronic conductivity and subsequently increase the charge transfer.[53] Smaller nanoparticles could also accelerate the oxygen loss in crystal structure, leading to high concentration of oxygen vacancy. With those characteristics, we predict that LSM and LSMI from our PACS method show better electrochemical catalytic activities.

To gain insight into the ORR activities of LSM and LSMI, cyclic voltammetry was first examined in the oxygen-saturated 0.1 M KOH electrolyte at a scan rate of 50 mV s^{-1}, as shown in Figure S10. Both LSM and LSMI appear a substantial reduction process around −0.05 V vs Ag/AgCl. Apparently, electrocatalytic activity toward ORR of LSMI is better than that of LSM with more positive ORR onset potential and higher cathodic current density. To further evaluate the ORR performance of the catalysts, rotating disk electrode (RDE) experiments were performed. CV cycles were further carried out in the same electrolyte at a scan rate of 50 mV s^{-1} and a rotating speed of 900 rpm to study the stability of LSMI catalyst, as presented in Figure S11. The onset potentials of LSMI at the 2nd, 100th, and 200th cycles are very close, but the limited current density is slightly decreased after 200 cycles; considering the continuous consumption of oxygen during cycles, the slight decrease of the limited current density is acceptable, which confirms that LSMI exhibited good cycle durability. The linear sweep voltammetry (LSV) curves of LSM, LSMI ,and the commercial Pt/C catalysts at a rotation speed of 1600 rpm and a scan rate of 5 mV s^{-1} are presented in Figure 3a. The onset potential of LSMI catalyst is around −0.05 V vs Ag/AgCl, which is only 30 mV negative shift from the Pt/C catalyst. Again, LSMI exhibited a more positive onset potential than LSM, which is associated with more oxygen vacancy in LSMI with A-deficiency and Ir-doping. The contribution of glassy carbon (GC) electrode was reported negligible under the same testing condition, and the electrochemical performance of the catalyst-loaded GC electrode was mainly dominated by the catalysts.[30] Therefore, the LSV profiles reflect directly the electrochemical activities of the catalysts. The limited current densities for Pt/C, LSMI, and LSM are 5.3, 4.1, and 3.5 mA cm^{-2} (Figure 3b), respectively. To further understand the ORR kinetics for the catalysts, the detailed study of RDE tests for LSM and LSMI at different rotation speeds (100−1600 rpm, Figure 3c and Figure S12) was carried out. The calculated electron transfer number from the slope of the Koutecky−Levich (K−L) plots at −0.6 V vs Ag/AgCl is 3.7 and 3.9 for LSM and LSMI (Figure 3d), respectively. The excellent ORR performance demonstrates that the four-electron ORR reaction ($O_2 + 2H_2O + 4e^- \rightarrow 4OH^-$) was controlled for both LSM and LSMI catalysts. The smaller particles of the catalysts can facilitate oxygen adsorption and charge transfer, resulting in dominant selectivity of the four-electron transfer electrochemical process. Hence, introducing A-site deficiency and Ir-doping in perovskite oxide effectively enhanced the ORR activity.

Since IrO_2 has been proved as one of the best OER catalysts in alkaline solution, thus Ir-doping to perovskite oxide is supposed to achieve high OER performance. OER activities for LSM and LSMI were therefore evaluated to explore their application as bifunctional oxygen electrocatalysts. The OER activity was recorded by LSV curves within the OER potential window, as shown in Figure 4a. The onset potential for LSMI (∼0.48 V vs Ag/AgCl) is much lower and almost 0.2 V negative shift than that for LSM (∼0.68 V vs Ag/AgCl), indicating that LSMI exhibited greater current density under the same potential range and better OER catalytic activity as compared with LSM. LSMI catalyst also demonstrated higher OER activity than $LaFeO_3$-based perovskite under the same experimental condition.[30] In addition, the enhanced kinetics of the LSMI catalyst toward OER activity was certified by the

DOI: 10.1021/acsami.7b06458
ACS Appl. Mater. Interfaces 2017, 9, 23820−23827

Tafel plot and electrochemical impedance spectroscopy (EIS) analysis. LSMI has a much smaller Tafel slope (Figure 4b), a smaller diameter of the semicircle in the EIS spectra (Figure 4c), and hence more rapid OER rates and better charge transfer ability than LSM. The detailed information on EIS for LSM at different applied potentials is displayed in Figure S13. The diameter of semicircle becomes smaller as increasing the applied potentials. Moreover, almost no semicircle was observed when the applied potential was 0.6 V, indicating no OER current at potential of 0.6 V. More interesting, the charger transfer resistance for LSM even at the potential of 0.9 V vs Ag/AgCl is still larger than that of LSMI at lower potential of 0.6 V vs Ag/AgCl, further demonstrating that LSMI has better charge transfer ability than LSM. The enhancement in OER performance for LSMI is more pronounced, thus introducing A-site deficiency and B-site Ir-doping in LSM not only improves ORR activity but also enhances OER activity to a great extent.

In order to distinguish the contributions from the A-site deficiency and Ir-doping, the A-site deficiency $(La_{0.8}Sr_{0.2})_{0.95}MnO_3$ (ALSM) was prepared as a control sample. The ORR and OER performances of LSM and ALSM are presented in Figure S14. The ALSM showed poor ORR but better OER activity. The half-wave potential of ALSM is about 100 mV lower than that of LSM. The formation of oxygen vacancy after introducing A-deficiency could benefit for the adsorption of OH^- and then subsequently increase the OER performance. But the enhancement of OER in ALSM is still limited comparing with other perovskite oxide-based OER catalyst. Therefore, LSMI with improved ORR and OER performances was mainly due to Ir-doping.

The potential difference between $E_{j=10}$ (the OER potential at 10 mA cm^{-2}) and E_{-1} (the ORR potential at −1 mA cm^{-2}) is an important factor to evaluate the electrochemical properties of catalyst. Smaller ΔE ($\Delta E = E_{-1} - E_{j=10}$) implies that the catalyst is close to the ideal oxygen electrode for OER and ORR. From Figure 4d and Table S2, the ΔE values are 0.81 and 1.06 V for LSMI and LSM, respectively. Smaller ΔE value for LSMI demonstrates that introducing A-site deficiency and Ir-doping can significantly improve the catalyst bifunctionality. In addition, the ΔE of LSMI is much smaller than the commercial Pt/C, IrO_2, RuO_2, and reported perovskite oxide catalysts (Table S2). The lowest ΔE of LSMI indicates that LSMI could be promising electrocatalyst in the application of metal−air battery, fuel cell, and solar fuel fields.[54−58]

In order to further characterize the durability of LSMI catalyst, the LSV runs for initial ORR and OER activities were recorded in 0.1 M KOH at a rotation speed of 1600 rpm. Then the constant potential ∼0.6 V vs Ag/AgCl was applied to LSMI electrode for 5 h. During the test, bubbles continuously release from the electrode, and the bubbles would separate the direct contact between electrolyte and active materials. Therefore, we manually removed bubbles on the glass carbon electrode, then the LSV runs for ORR and OER after 5 h were performed again, as shown in Figure 4e,f. Compared with initial ORR, only 18 mV negative shift was detected for the half-wave potential while only 10% decay for the OER performance, meaning that LSMI exhibited high durability.

4. CONCLUSION

Perovskite oxide LSM and LSMI nanoparticles with particle size of 20−50 nm are prepared and applied as high performance bifunctional catalyst in alkaline solution. Electrochemical results indicate that the ORR and OER activities are enhanced by the A-site deficiency and B-site Ir-doping in LSM-based perovskite. Partial reduction of the valence state of Mn could weaken its bonding with oxygenate adsorbate intermediate, and more oxygen vacancy would enhance the electrochemical performance. The significant enhancement in electrocatalytic activity (0.2 V negative shift for the onset potential as compared with LSM) could be observed in the OER process while LSMI reported the superior ORR performance (only 30 mV difference from the commercial Pt/C catalyst). The ΔE value of LSMI (∼0.81 V) compares favorably with some other perovskite-based bifunctional catalysts reported in the literature. The durability investigation demonstrated only 18 mV shift for ORR and 10% decay for OER. These results prove that LSMI could be a promising catalyst for the applications in fuel cells, metal−air batteries, and solar fuel synthesis.

■ ASSOCIATED CONTENT

Ⓢ Supporting Information

The Supporting Information is available free of charge on the ACS Publications website at DOI: 10.1021/acsami.7b06458.

> Figure S1: XRD Rietveld refinement for LSMI; Figure S2: XPS spectra for LSM and LSMI; Figure S3: high-resolution XPS spectrum for Ir in LSMI; Figure S4: high-resolution XPS spectra for oxygen in LSM and LSMI; Figure S5: TEM images and SAED pattern of LSM; Figure S6: nitrogen adsorption and desorption profile of LSMI; Figure S7: SEM images of LSMI; Figure S8: molecular structure of EDTA and PEI and the bonding with transition metal ions; Figure S9: TEM image of carbon-coated LSMI heated at 550 °C; Figure S10: cyclic voltammetry curves of LSM and LSMI catalysts in oxygen-saturated 0.1 M KOH electrolyte at a scan rate of 50 mV s^{-1}; Figure S11: CVs of LSMI in oxygen-saturated 0.1 M KOH electrolyte at a scan rate of 50 mV/s and a rotating speed of 900 rpm; Figure S12: LSV profiles for LSM at different rotation speeds; Figure S13: EIS spectra of LSM at different applied potentials; Figure S14: ORR and OER performances of LSM and ALSM; Table S1: concentrations of the different kinds of the valence state of Mn estimated from the relative area of the fitted subpeaks for LSM and LSMI; Table S2: comparison of the bifunctional catalytic activity for LSM and LSMI catalyst, noble-metal-based and some other reported perovskite-based bifunctional catalysts in the literature (PDF)

■ AUTHOR INFORMATION

Corresponding Authors

*Tel 575-646-4204, Fax 575-646-7706, e-mail hluo@nmsu.edu (H.L.).
*Tel 575-646-1018, Fax 575-646-7706, e-mail mzhou@nmsu.edu (M.Z.).

ORCID

Hongmei Luo: 0000-0002-9546-761X

Author Contributions

L.Y. and Y.L. contributed equally to this work.

Notes

The authors declare no competing financial interest.

ACKNOWLEDGMENTS

Dr. Luo thanks the support from New Mexico EPSCoR (NSF-1301346), the USDA National Institute of Food and Agriculture, and HSI Collaboration: Integrating Food Science/Engineering and Education Network (IFSEEN, Award 2015-38422-24059). Dr. Lin thanks the support of the Young Scientists Fund of the National Natural Science Foundation of China (11404314), Anhui Provincial Natural Science Foundation (1708085MA06), and the Fundamental Research Funds for the Central Universities (WK2340000055). Dr. Yu acknowledges the support from the China Scholarship Council. T.S., a senior at Onate High School, and H.S., a senior at Mayfield High School, participated in the Las Cruces Public School EXCEL program.

REFERENCES

(1) Chen, G.; Yan, L.; Luo, H.; Guo, S. Nanoscale Engineering of Heterostructured Anode Materials for Boosting Lithium-Ion Storage. *Adv. Mater.* **2016**, *28*, 7580−7602.

(2) Yan, L.; Rui, X.; Chen, G.; Xu, W.; Zou, G.; Luo, H. Recent Advances in Nanostructured Nb-based Oxides for Electrochemical Energy Storage. *Nanoscale* **2016**, *8*, 8443−8465.

(3) Aricò, A. S.; Siracusano, S.; Briguglio, N.; Baglio, V.; Di Blasi, A.; Antonucci, V. Polymer Electrolyte Membrane Water Electrolysis: Status of Technologies and Potential Applications in Combination with Renewable Power Sources. *J. Appl. Electrochem.* **2013**, *43*, 107−118.

(4) Yan, L.; Chen, G.; Tan, S.; Zhou, M.; Zou, G.; Deng, S.; Smirnov, S.; Luo, H. Titanium Oxynitride Nanoparticles Anchored on Carbon Nanotubes as Energy Storage Materials. *ACS Appl. Mater. Interfaces* **2015**, *7*, 24212−24217.

(5) Kadakia, K.; Datta, M. K.; Jampani, P. H.; Park, S. K.; Kumta, P. N. Novel F-doped IrO_2 Oxygen Evolution Electrocatalyst for PEM Based Water Electrolysis. *J. Power Sources* **2013**, *222*, 313−317.

(6) Bockris, J. O. M.; Otagawa, T. The Electrocatalysis of Oxygen Evolution on Perovskites. *J. Electrochem. Soc.* **1984**, *131*, 290−302.

(7) Bockris, J. O.; Otagawa, T. Mechanism of Oxygen Evolution on Perovskites. *J. Phys. Chem.* **1983**, *87*, 2960−2971.

(8) Reier, T.; Oezaslan, M.; Strasser, P. Electrocatalytic Oxygen Evolution Reaction (OER) on Ru, Ir, and Pt Catalysts: A Comparative Study of Nanoparticles and Bulk Materials. *ACS Catal.* **2012**, *2*, 1765−1772.

(9) Takenaka, H.; Torikai, E.; Kawami, Y.; Wakabayashi, N. Solid Polymer Electrolyte Water Electrolysis. *Int. J. Hydrogen Energy* **1982**, *7*, 397−403.

(10) Amiinu, I. S.; Zhang, J.; Kou, Z.; Liu, X.; Asare, O. K.; Zhou, H.; Cheng, K.; Zhang, H.; Mai, L.; Pan, M.; Mu, S. Self-Organized 3D Porous Graphene Dual-Doped with Biomass-Sponsored Nitrogen and Sulfur for Oxygen Reduction and Evolution. *ACS Appl. Mater. Interfaces* **2016**, *8*, 29408−29418.

(11) Millet, P.; Mbemba, N.; Grigoriev, S. A.; Fateev, V. N.; Aukauloo, A.; Etiévant, C. Electrochemical Performances of PEM Water Electrolysis Cells and Perspectives. *Int. J. Hydrogen Energy* **2011**, *36*, 4134−4142.

(12) Malkhandi, S.; Trinh, P.; Manohar, A. K.; Manivannan, A.; Balasubramanian, M.; Prakash, G. K. S.; Narayanan, S. R. Design Insights for Tuning the Electrocatalytic Activity of Perovskite Oxides for the Oxygen Evolution Reaction. *J. Phys. Chem. C* **2015**, *119*, 8004−8013.

(13) Zhao, S.; Yu, H.; Maric, R.; Danilovic, N.; Capuano, C. B.; Ayers, K. E.; Mustain, W. E. Calculating the Electrochemically Active Surface Area of Iridium Oxide in Operating Proton Exchange Membrane Electrolyzers. *J. Electrochem. Soc.* **2015**, *162*, F1292−F1298.

(14) Ji, L.; Meduri, P.; Agubra, V.; Xiao, X.; Alcoutlabi, M. Graphene-Based Nanocomposites for Energy Storage. *Adv. Energy Mater.* **2016**, *6*, 1502159.

(15) Zhao, Y.; Xu, L.; Mai, L.; Han, C.; An, Q.; Xu, X.; Liu, X.; Zhang, Q. Hierarchical Mesoporous Perovskite $La_{0.5}Sr_{0.5}CoO_{2.91}$ Nanowires with Ultrahigh Capacity for Li-Air Batteries. *Proc. Natl. Acad. Sci. U. S. A.* **2012**, *109*, 19569−19574.

(16) Cheng, F.; Chen, J. Metal-air Batteries: From Oxygen Reduction Electrochemistry to Cathode Catalysts. *Chem. Soc. Rev.* **2012**, *41*, 2172−2192.

(17) Takeguchi, T.; Yamanaka, T.; Takahashi, H.; Watanabe, H.; Kuroki, T.; Nakanishi, H.; Orikasa, Y.; Uchimoto, Y.; Takano, H.; Ohguri, N.; Matsuda, M.; Murota, T.; Uosaki, K.; Ueda, W. Layered Perovskite Oxide: A Reversible Air Electrode for Oxygen Evolution/Reduction in Rechargeable Metal-Air Batteries. *J. Am. Chem. Soc.* **2013**, *135*, 11125−11130.

(18) Xu, J.-J.; Xu, D.; Wang, Z.-L.; Wang, H.-G.; Zhang, L.-L.; Zhang, X.-B. Synthesis of Perovskite-Based Porous $La_{0.75}Sr_{0.25}MnO_3$ Nanotubes as a Highly Efficient Electrocatalyst for Rechargeable Lithium−Oxygen Batteries. *Angew. Chem., Int. Ed.* **2013**, *52*, 3887−3890.

(19) Suntivich, J.; May, K. J.; Gasteiger, H. A.; Goodenough, J. B.; Shao-Horn, Y. A Perovskite Oxide Optimized for Oxygen Evolution Catalysis from Molecular Orbital Principles. *Science* **2011**, *334*, 1383−1385.

(20) Fuentes, R. E.; Farell, J.; Weidner, J. W. Multimetallic Electrocatalysts of Pt, Ru, and Ir Supported on Anatase and Rutile TiO_2 for Oxygen Evolution in an Acid Environment. *Electrochem. Solid-State Lett.* **2011**, *14*, E5−E7.

(21) Zhou, W.; Wu, X.-J.; Cao, X.; Huang, X.; Tan, C.; Tian, J.; Liu, H.; Wang, J.; Zhang, H. Ni_3S_2 nanorods/Ni Foam Composite Electrode with Low Overpotential for Electrocatalytic Oxygen Evolution. *Energy Environ. Sci.* **2013**, *6*, 2921−2924.

(22) Qu, L.; Liu, Y.; Baek, J.-B.; Dai, L. Nitrogen-Doped Graphene as Efficient Metal-Free Electrocatalyst for Oxygen Reduction in Fuel Cells. *ACS Nano* **2010**, *4*, 1321−1326.

(23) Zhao, S.; Rasimick, B.; Mustain, W.; Xu, H. Highly Durable and Active Co_3O_4 Nanocrystals Supported on Carbon Nanotubes as Bifunctional Electrocatalysts in Alkaline Media. *Appl. Catal., B* **2017**, *203*, 138−145.

(24) Gupta, S.; Qiao, L.; Zhao, S.; Xu, H.; Lin, Y.; Devaguptapu, S. V.; Wang, X.; Swihart, M. T.; Wu, G. Highly Active and Stable Graphene Tubes Decorated with FeCoNi Alloy Nanoparticles via a Template-Free Graphitization for Bifunctional Oxygen Reduction and Evolution. *Adv. Energy Mater.* **2016**, *6*, 1601198.

(25) Suntivich, J.; Gasteiger, H. A.; Yabuuchi, N.; Nakanishi, H.; Goodenough, J. B.; Shao-Horn, Y. Design Principles for Oxygen-reduction Activity on Perovskite Oxide Catalysts for Fuel Cells and Metal−Air Batteries. *Nat. Chem.* **2011**, *3*, 546−550.

(26) Jin, C.; Cao, X.; Lu, F.; Yang, Z.; Yang, R. Electrochemical Study of $Ba_{0.5}Sr_{0.5}Co_{0.8}Fe_{0.2}O_3$ Perovskite as Bifunctional Catalyst in Alkaline Media. *Int. J. Hydrogen Energy* **2013**, *38*, 10389−10393.

(27) Jin, C.; Yang, Z.; Cao, X.; Lu, F.; Yang, R. A Novel Bifunctional Catalyst of $Ba_{0.9}Co_{0.5}Fe_{0.4}Nb_{0.1}O_{3-\delta}$ Perovskite for Lithium−air Battery. *Int. J. Hydrogen Energy* **2014**, *39*, 2526−2530.

(28) Mefford, J. T.; Rong, X.; Abakumov, A. M.; Hardin, W. G.; Dai, S.; Kolpak, A. M.; Johnston, K. P.; Stevenson, K. J. Water Electrolysis on $La_{1-x}Sr_xCoO_{3-\delta}$ Perovskite Electrocatalysts. *Nat. Commun.* **2016**, *7*, 11053.

(29) Peña, M. A.; Fierro, J. L. G. Chemical Structures and Performance of Perovskite Oxides. *Chem. Rev.* **2001**, *101*, 1981−2018.

(30) Zhu, Y.; Zhou, W.; Yu, J.; Chen, Y.; Liu, M.; Shao, Z. Enhancing Electrocatalytic Activity of Perovskite Oxides by Tuning Cation Deficiency for Oxygen Reduction and Evolution Reactions. *Chem. Mater.* **2016**, *28*, 1691−1697.

(31) Jung, J.-I.; Risch, M.; Park, S.; Kim, M. G.; Nam, G.; Jeong, H.-Y.; Shao-Horn, Y.; Cho, J. Optimizing Nanoparticle Perovskite for Bifunctional Oxygen Electrocatalysis. *Energy Environ. Sci.* **2016**, *9*, 176−183.

(32) Gupta, S.; Kellogg, W.; Xu, H.; Liu, X.; Cho, J.; Wu, G. Bifunctional Perovskite Oxide Catalysts for Oxygen Reduction and Evolution in Alkaline Media. *Chem. - Asian J.* **2016**, *11*, 10−21.

(33) Zhou, S.; Miao, X.; Zhao, X.; Ma, C.; Qiu, Y.; Hu, Z.; Zhao, J.; Shi, L.; Zeng, J. Engineering Electrocatalytic Activity in Nanosized Perovskite Cobaltite Through Surface Spin-state Transition. *Nat. Commun.* **2016**, *7*, 11510.

(34) Lin, Q.; Xu, Y.; Fu, E.; Baber, S.; Bao, Z.; Yu, L.; Deng, S.; Kundu, J.; Hollingsworth, J.; Bauer, E.; McCleskey, T. M.; Burrell, A. K.; Jia, Q.; Luo, H. Polymer-Assisted Chemical Solution Approach to YVO_4:Eu Nanoparticle Networks. *J. Mater. Chem.* **2012**, *22*, 5835−5839.

(35) Kostogloudis, G. C.; Ftikos, C. Properties of A-Site-Deficient $La_{0.6}Sr_{0.4}Co_{0.2}Fe_{0.8}O_{3-\delta}$-based Perovskite Oxides. *Solid State Ionics* **1999**, *126*, 143−151.

(36) Lein, H. L.; Wiik, K.; Grande, T. Thermal and Chemical Expansion of Mixed Conducting $La_{0.5}Sr_{0.5}Fe_{1-x}Co_xO_{3-\delta}$ Materials. *Solid State Ionics* **2006**, *177*, 1795−1798.

(37) Juste, E.; Julian, A.; Etchegoyen, G.; Geffroy, P. M.; Chartier, T.; Richet, N.; Del Gallo, P. Oxygen Permeation, Thermal and Chemical Expansion of (La,Sr)(Fe, Ga)$O_{3-\delta}$ Perovskite Membranes. *J. Membr. Sci.* **2008**, *319*, 185−191.

(38) Giri, A.; Goswami, N.; Bootharaju, M. S.; Xavier, P. L.; John, R.; Thanh, N. T. K.; Pradeep, T.; Ghosh, B.; Raychaudhuri, A. K.; Pal, S. K. Emergence of Multicolor Photoluminescence in $La_{0.67}Sr_{0.33}MnO_3$ Nanoparticles. *J. Phys. Chem. C* **2012**, *116*, 25623−25629.

(39) Zhang, C.; Berlinguette, C. P.; Trudel, S. Water Oxidation Catalysis: An Amorphous Quaternary Ba-Sr-Co-Fe Oxide as a Promising Electrocatalyst for the Oxygen-Evolution Reaction. *Chem. Commun.* **2016**, *52*, 1513−1516.

(40) Miyahara, Y.; Miyazaki, K.; Fukutsuka, T.; Abe, T. Influence of Surface Orientation on the Catalytic Activities of $La_{0.8}Sr_{0.2}CoO_3$ Crystal Electrodes for Oxygen Reduction and Evolution Reactions. *ChemElectroChem.* **2016**, *3*, 214−217.

(41) Vojvodic, A.; Nørskov, J. K. Optimizing Perovskites for the Water-Splitting Reaction. *Science* **2011**, *334*, 1355−1356.

(42) Li, Y.-F.; Selloni, A. Mechanism and Activity of Water Oxidation on Selected Surfaces of Pure and Fe-Doped NiO_x. *ACS Catal.* **2014**, *4*, 1148−1153.

(43) Bajdich, M.; García-Mota, M.; Vojvodic, A.; Nørskov, J. K.; Bell, A. T. Theoretical Investigation of the Activity of Cobalt Oxides for the Electrochemical Oxidation of Water. *J. Am. Chem. Soc.* **2013**, *135*, 13521−13530.

(44) Plaisance, C. P.; van Santen, R. A. Structure Sensitivity of the Oxygen Evolution Reaction Catalyzed by Cobalt(II,III) Oxide. *J. Am. Chem. Soc.* **2015**, *137*, 14660−14672.

(45) Rincón, R. A.; Ventosa, E.; Tietz, F.; Masa, J.; Seisel, S.; Kuznetsov, V.; Schuhmann, W. Evaluation of Perovskites as Electrocatalysts for the Oxygen Evolution Reaction. *ChemPhysChem* **2014**, *15*, 2810−2816.

(46) Han, B.; Stoerzinger, K. A.; Tileli, V.; Gamalski, A. D.; Stach, E. A.; Shao-Horn, Y. Nanoscale Structural Oscillations in Perovskite Oxides Induced by Oxygen Evolution. *Nat. Mater.* **2016**, *16*, 121−126.

(47) Guo, Y.; Tong, Y.; Chen, P.; Xu, K.; Zhao, J.; Lin, Y.; Chu, W.; Peng, Z.; Wu, C.; Xie, Y. Engineering the Electronic State of a Perovskite Electrocatalyst for Synergistically Enhanced Oxygen Evolution Reaction. *Adv. Mater.* **2015**, *27*, 5989−5994.

(48) Zhu, Y.; Zhou, W.; Chen, Y.; Yu, J.; Xu, X.; Su, C.; Tadé, M. O.; Shao, Z. Boosting Oxygen Reduction Reaction Activity of Palladium by Stabilizing Its Unusual Oxidation States in Perovskite. *Chem. Mater.* **2015**, *27*, 3048−3054.

(49) Burrell, A. K.; Mark McCleskey, T.; Jia, Q. X. Polymer Assisted Deposition. *Chem. Commun.* **2008**, 1271−1277.

(50) Zou, G. F.; Zhao, J.; Luo, H. M.; McCleskey, T. M.; Burrell, A. K.; Jia, Q. X. Polymer-Assisted-Deposition: A Chemical Solution Route for a Wide Range of Materials. *Chem. Soc. Rev.* **2013**, *42*, 439−449.

(51) Jiang, Y.; Chen, G.; Xu, X.; Chen, X.; Deng, S.; Smirnov, S.; Luo, H.; Zou, G. Direct Growth of Mesoporous Anatase TiO_2 on Nickel Foam by Soft Template Method as Binder-Free Anode for Lithium-Ion Batteries. *RSC Adv.* **2014**, *4*, 48938−48942.

(52) Xu, Y.; Fei, L.; Fu, E.; Yuan, B.; Hill, J.; Chen, Y.; Deng, S.; Andersen, P.; Wang, Y.; Luo, H. A General Polymer-Assisted Solution Approach to Grow Transition Metal Oxide Nanostructures Directly on Nickel Foam as Anodes for Li-Ion Batteries. *J. Power Sources* **2013**, *242*, 604−609.

(53) Ge, X.; Sumboja, A.; Wuu, D.; An, T.; Li, B.; Goh, F. W. T.; Hor, T. S. A.; Zong, Y.; Liu, Z. Oxygen Reduction in Alkaline Media: From Mechanisms to Recent Advances of Catalysts. *ACS Catal.* **2015**, *5*, 4643−4667.

(54) Jin, C.; Cao, X.; Zhang, L.; Zhang, C.; Yang, R. Preparation and Electrochemical Properties of Urchin-like $La_{0.8}Sr_{0.2}MnO_3$ Perovskite Oxide as a Bifunctional Catalyst for Oxygen Reduction and Oxygen Evolution Reaction. *J. Power Sources* **2013**, *241*, 225−230.

(55) Lu, F.; Wang, Y.; Jin, C.; Li, F.; Yang, R.; Chen, F. Microporous $La_{0.8}Sr_{0.2}MnO_3$ Perovskite Nanorods as Efficient Electrocatalysts for Lithium−Air Battery. *J. Power Sources* **2015**, *293*, 726−733.

(56) Cao, X.; Wu, J.; Jin, C.; Tian, J.; Strasser, P.; Yang, R. $MnCo_2O_4$ Anchored on P-Doped Hierarchical Porous Carbon as an Electrocatalyst for High-Performance Rechargeable Li−O_2 Batteries. *ACS Catal.* **2015**, *5*, 4890−4896.

(57) Jin, C.; Lu, F.; Cao, X.; Yang, Z.; Yang, R. Facile Synthesis and Excellent Electrochemical Properties of $NiCo_2O_4$ Spinel Nanowire Arrays as a Bifunctional Catalyst for the Oxygen Reduction and Evolution Reaction. *J. Mater. Chem. A* **2013**, *1*, 12170−12177.

(58) Lu, F.; Cao, X.; Wang, Y.; Jin, C.; Shen, M.; Yang, R. A Hierarchical $NiCo_2O_4$ Spinel Nanowire Array as an Electrocatalyst for Rechargeable Li-Air Batteries. *RSC Adv.* **2014**, *4*, 40373−40376.